Enhanced Photovoltaic Performance of Nanowire Dye-Sensitized Solar Cells Based on Coaxial TiO$_2$@TiO Heterostructures with a Cobalt(II/III) Redox Electrolyte

Jiandong Fan,[†] Cristian Fàbrega,*[,†] Reza R. Zamani,[†,‡] Yan Hao,[§] Andres Parra,[†] Teresa Andreu,[†] Jordi Arbiol,[‡,⊥] Gerrit Boschloo,[§] Anders Hagfeldt,[§] Joan Ramon Morante,[†,∥] and Andreu Cabot*[,†,∥]

[†]Catalonia Institute for Energy Research (IREC), Sant Adrià de Besòs 08930, Spain
[∥]Departament d'Electrònica, Universitat de Barcelona, Barcelona 08028, Spain
[‡]Institut de Ciencia de Materials de Barcelona, ICMAB-CSIC, Campus de la UAB, Bellaterra 08193, Spain
[§]Ångström Laboratory, Department of Chemistry, Uppsala University, Box 523, 75120 Uppsala, Sweden
[⊥]Institució Catalana de Recerca i Estudis Avançats (ICREA), Barcelona 08010, Spain

ABSTRACT: The growth of a TiO shell at the surface of TiO$_2$ nanowires (NWs) allowed us to improve the power conversion efficiency of NW-based dye-sensitized solar cells (DSCs) by a factor 2.5. TiO$_2$@TiO core−shell NWs were obtained by a two-step process: First, rutile-phase TiO$_2$ NWs were hydrothermally grown. Second, a hongquiite-phase TiO shell was electrochemically deposited at the surface of the TiO$_2$ NWs. Bare TiO$_2$ and heterojunction TiO$_2$@TiO NW-based DSCs were obtained using a cobalt(II/III) redox electrolyte and LEG4 as the dye. With this electrolyte/dye combination, DSCs with outstanding V_{oc} values above 900 mV were systematically obtained. While TiO$_2$@TiO NW-based DSCs had slightly lower V_{oc} values than bare TiO$_2$ NW-based DSCs, they provided 3-fold higher photocurrents, overall reaching 2.5-fold higher power conversion efficiencies. The higher photocurrents were associated with the larger surface roughness and an enhanced charge-carrier separation/transfer at the NW/dye interface.

KEYWORDS: hydrothermal deposition, electrochemical deposition, nanowires, TiO$_2$, cobalt(II/III) electrolyte, dye-sensitized solar cells
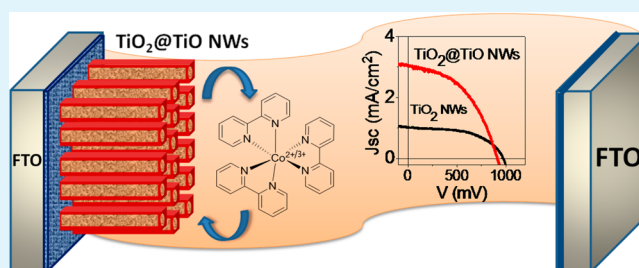
INTRODUCTION

Oriented one-dimensional nanostructures with direct charge-transport paths from reaction/injection sites to the electrode are excellent architectures to improve efficiency in multiple electrocatalytic, electronic, and optoelectronic applications.[1−3] While the nanowire (NW) geometry habilitates the combined optimization of both charge-carrier transport and charge-carrier injection/separation, its composition also needs to satisfy strong demands in terms of the surface chemistry and electrical transport properties. In this scenario, core−shell nanostructures permit one to independently optimize both processes and to further take advantage of the synergic combination of two different materials.[4−7]

TiO$_2$ NWs find numerous technological uses, e.g., gas sensing,[8,9] photovoltaics,[10,11] photodetection,[12] photocatalysis,[13,14] and photoelectrocatalysis.[15,16] In all of these applications, TiO$_2$ plays multiple roles: (i) it supports the photoactive or catalytically active species; (ii) it plays a catalytic/photocatalytic role itself; (iii) it collects/separates charge carriers from photoactive or catalytically active sites and species; (iv) it provides avenues for charge-carrier transportation between reaction sites or between reaction/photogeneration/recombination sites and the electrodes. Such

multifunctional character requires very demanding material qualities, for which independent optimization is frequently incompatible with the limited degrees of freedom available in a single material.

Compositionally graded and core−shell nanostructures are interesting architectures able to provide higher levels of control over the material's functional properties.[17−19] Shells can provide higher chemical stability and surface passivation to prevent recombination, and they can extend the electric field region for charge-carrier separation.[4−6] Shells of lower-band-gap materials are also able to extend the NW's core optical absorption to lower energies, thus promoting charge-carrier photogeneration.[20−22]

However, to grow defect-free coaxial heterojunctions, a major challenge needs to be overcome: the lattice mismatch.[23] Lattice mismatches generally introduce a significant density of interface defects that strongly deteriorate the optoelectronic properties of the formed heterostructure.

In this letter, we detail a low-cost, high-yield, and easily scalable electrochemical deposition process to epitaxially grow a cubic hongquiite TiO shell on the surface of single-crystal rutile TiO_2 NWs. To assess the potential of the coaxial TiO_2@TiO NW architecture, dye-sensitized solar cells (DSCs) were fabricated and characterized.

EXPERIMENTAL SECTION

Rutile TiO_2 NWs. Titania NWs with the rutile crystal phase were hydrothermally grown over a conductive substrate (2×2 cm^2 FTO-coated glass pieces).[10,24] Briefly, we filled a teflon-lined stainless steel autoclave (125 mL, Parr Instrument Co.) with 60 mL of a 6 M HCl (37 % PaNWeac) solution and 1 mL of titanium butoxide (Fluka). The reactor was heated to 200 °C and kept at this temperature for 4 h. Afterward, it was cooled to room temperature with the help of a water bath. The as-prepared samples were cleaned by sonication in water, dried under a nitrogen flow, and finally annealed at 450 °C in an oxygen atmosphere for 1 h in order to remove any residues from the synthetic process.[25]

TiO_2@TiO Core–Shell NWs. A TiO shell was electro-deposited on the surface of TiO_2 NWs using a PARSTAT 2733 (Princeton Applied Research). The precursor solution consisted of $TiCl_3$ (10%) in HCl (20−30%) with a pH adjusted to 2.7 with Na_2CO_3 (1.9 M). Nitrogen was bubbled through the solution for 1 h prior to deposition. Electro-deposition was performed at a constant voltage (0.0 V vs Ag/AgCl) and temperature (25 °C) for 30 s. The as-prepared samples were cleaned by sonication in water, dried under a nitrogen flow, and finally annealed at 450 °C in an oxygen atmosphere for 2 h.

DSCs Fabrication. Dye uptake was carried out by immersing the TiO_2 NW photoanodes (0.25 cm^2) into an ethanol solution (0.2 mM) of LEG4 (Figure 1) at room temperature for 20 h. A platinum-coated counter electrode was prepared by drop-casting a 5 mM H_2PtCl_6/ethanol solution onto an FTO-coated glass, followed by sintering at 450 °C in

air for 30 min. A 25-μm-thick hot-melted film (Solaronix) was sandwiched between the TiO_2 NW-based photoanodes and platinum counter electrode. To complete the device, the $[Co(bpy)_3]^{2+/3+}$ electrolyte was injected into the space between the cell's anode and cathode through a hole drilled on the counter electrode. The electrolyte was obtained by mixing 0.22 M $Co(bpy)_3(PF_6)_2$, 0.05 M $Co(bpy)_3(PF_6)_3$, 0.1 M $LiClO_4$, and 0.2 M 4-*tert*-butylpyridine in acetonitrile.[26,27]

Characterization. X-ray diffraction (XRD) patterns were obtained with Cu Kα ($\lambda = 1.5406$ Å) radiation in reflection geometry on a Bruker D8 operating at 40 kV and 40 mA. The morphology of TiO_2 NW arrays was characterized by field-emission scanning electron microscopy (FESEM; Zeiss Serie Auriga). The morphology and crystallographic structure of TiO_2@TiO core−shell NWs were further characterized with atomic resolution by means of high-resolution transmission electron microscopy (HRTEM) in a Jeol 2010F field-emission gun microscope with a 0.19 nm point-to-point resolution. Electron energy loss spectroscopy (EELS) was carried out on the same microscope in order to confirm the chemical composition.

Current−voltage ($J–V$) characteristics were measured using a Keithley 2400 source/meter and a Newport solar simulator (model 91160) with AM 1.5G spectral distribution. The intensity power was adjusted to 1000 W/m^2 using a certified reference solar cell (Fraunhofer ISE). A black mask with an aperture of 0.5×0.5 cm^2 was placed on top of the cell to avoid any significant contribution from outside of the active area. Incident photon-to-current conversion efficiency (IPCE) spectra were recorded using a computer-controlled setup consisting of a xenon light source (Spectral Products ASBXE-175), a monochromator (Spectral Products CM110), and a potentiostat (EG&G PAR 273), calibrated using a certified reference solar cell (Fraunhofer ISE).

RESULTS AND DISCUSSION

Figure 2a shows representative FESEM images of the TiO_2 nanostructures grown by the above-detailed hydrothermal process onto FTO-covered glass substrates. The TiO_2 NWs obtained by the described hydrothermal process were 150 nm thick and 3 μm long, and they were characterized by smooth surfaces (Figure 2a,c). Electrodeposition, suitable for coating very high aspect ratio nanostructures, was the technique used to grow the titanium oxide shell. After electrochemical deposition of the shell, the NW surface became significantly rougher (Figure 2b). Extensive FESEM characterization demonstrated full coverage of the TiO_2 NW surface.

Individual core−shell NWs were further analyzed by means of HRTEM and EELS to determine the core and shell crystallographic phases and compositions. As expected, the core crystallized in the rutile phase (Figure 3a,c). On the other hand, the electrodeposited shell displayed a cubic TiO crystal structure known as hongquiite (Figure 3a,b).[28] Power spectral (fast Fourier transform, FFT) analyses (Figure 3d,e) revealed the perfect epitaxy between hongquiite TiO and rutile TiO_2 because the (2−20) plane family of hongquiite is almost equal to the (002) plane family of rutile. This epitaxial growth is favored by the very similar lattice parameters of both structures in these two directions: the plane distance difference between rutile (001), 2.956 Å, and hongquiite (1−10), 2.953 Å, is only 0.003 Å (about 0.1%). In the filtered HRTEM magnified detail shown in Figure 3d, the two titanium oxide structures are clearly exhibited. At the very surface of the NW, an amorphous
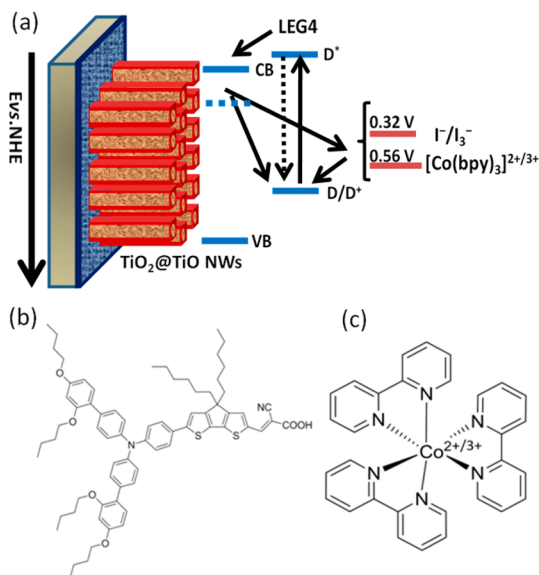

Figure 1. (a) Schematic energy diagram of a TiO_2 NW solar cell sensitized with LEG4 and using I^-/I_3^- or $[Co(bpy)_3]^{2+/3+}$ as the electrolyte. (b) Molecular structure of the LEG4 dye. (c) Molecular structure of $[Co(bpy)_3]^{2+/3+}$.
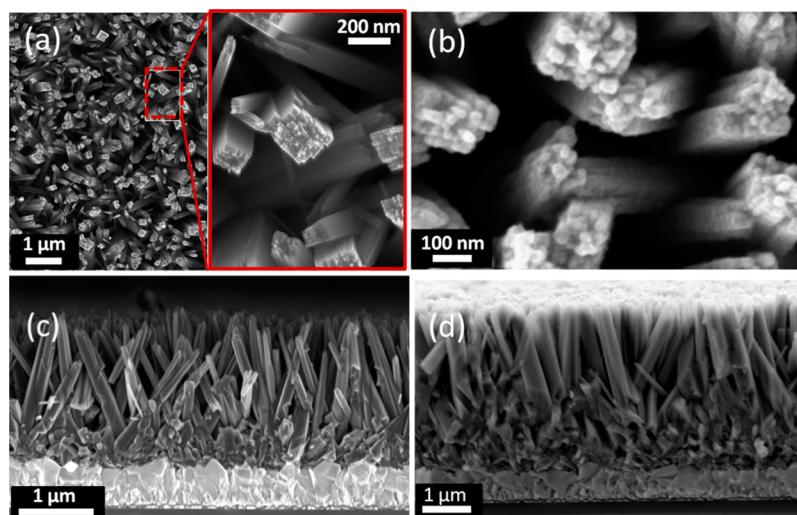
Figure 2. Top-down SEM images of (a) bare rutile TiO_2 NWs and (b) TiO_2@TiO core−shell NWs. Cross-sectional SEM images of (c) bare rutile TiO_2 NWs and (d) TiO_2@TiO core−shell NWs.
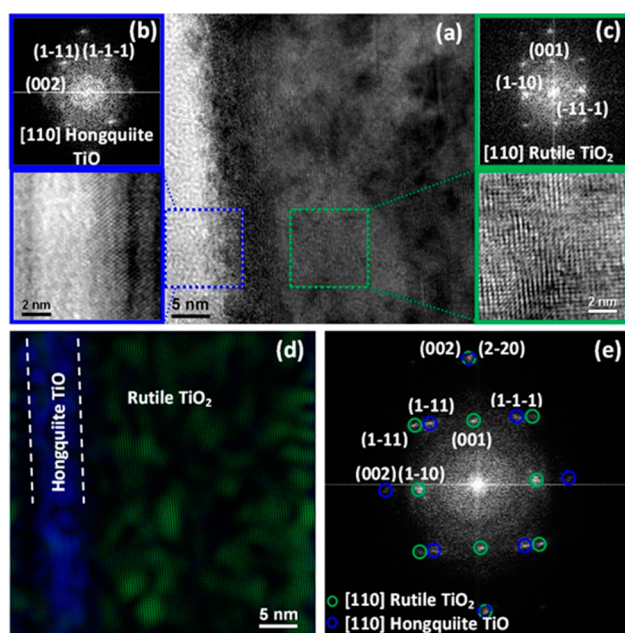

Figure 3. (a) HRTEM micrograph of a single TiO_2@TiO core−shell NW, with magnified zones in blue and green showing (b) hongquiite TiO and (c) rutile TiO_2, associated with corresponding power spectra (FFT). (d) HRTEM magnified detail obtained by filtering the power spectrum (e) of the HRTEM micrograph (a).

thin layer is also intuited, which we associate with a disordered titanium oxide. X-ray photoelectron spectroscopy analysis confirmed the outermost surface layer of the NW to be fully oxidized and covered by adsorbed oxygen and oxygen-containing species.

EELS analysis further confirmed the results obtained by HRTEM. As seen in the EELS profile (Figure 4), the percentage of titanium versus oxygen increased at the NW edge, which is consistent with the identification of the shell with the hongquiite-phase TiO. While the relative composition at the NW center was 33 ± 4% titanium and 66 ± 4% oxygen, at the surface, the titanium percentage increased to 41%. It needs to be taken into account that the e-beam probes a region of a few nanometers and that the very surface of the NWs is most

probably fully oxidized and covered by adsorbed oxygen-containing species. From these analyses, the thickness of the TiO shell was estimated to be 6 nm and the thickness of the amorphous outermost surface layer to be around 2 nm.

The crystallographic phases within TiO_2@TiO NWs were further confirmed by XRD. As shown in Figure 5a, the XRD patterns of bare rutile TiO_2 NWs were consistent with those of the rutile TiO_2 phase. After the shell was grown, the XRD patterns of the TiO_2@TiO NWs clearly displayed the (200) peak corresponding to the cubic hongquiite-phase TiO (inset of Figure 5a).

TiO_2 and TiO_2@TiO NW-based DSCs were fabricated using the $[Co(bpy)_3]^{2+/3+}$ redox shuttle as the electrolyte and LEG4 as the dye. Figure 6 displays the $J-V$ characteristic and IPCE of TiO_2 and TiO_2@TiO NW-based DSCs. Table 1 summarizes the measured photovoltaic parameters. DSCs based on bare rutile TiO_2 NWs showed photocurrents (J_{sc}) around 1.0 mA/cm^2, an open-circuit voltage (V_{oc}) of 975 mV, and power conversion efficiencies around 0.5%. The outstanding V_{oc} values obtained were associated with the use of $[Co(bpy)_3]^{2+/3+}$ as the electrolyte. Cobalt(III/II) redox complexes have been demonstrated as excellent alternatives to the I^-/I_3^- redox couple in TiO_2-based DSCs because they can minimize energy loss in the dye regeneration step (Figure 1).[26,27,29,30] V_{oc} values of equivalent solar cells fabricated using the I^-/I_3^- electrolyte were limited to values around 650 mV.[10,31]

With the presence of the hongquiite TiO shell, TiO_2@TiO NW-based DSCs showed significantly higher J_{sc} values. A 3-fold increase in J_{sc}, up to values above 3.0 mA/cm^2, was systematically obtained. On the other hand, V_{oc} values were just slightly reduced, down to 915 mV. Overall, with the presence of the TiO shell, the overall DSC conversion efficiency increased by a factor 2.5, up to 1.3%.

With the use of coaxial TiO_2@TiO core−shell NWs, a notable IPCE enhancement was observed in the visible part of the spectra (Figure 6b). The J_{sc} increase and related higher efficiencies obtained when using TiO_2@TiO NWs instead of bare TiO_2 NWs were partially associated with the higher dye loading. After the exact same dye loading process, the color of TiO_2@TiO core−shell NW arrays was significantly deeper than that of TiO_2 NWs. Figure 5b shows the UV−vis absorbance spectra of TiO_2@TiO and TiO_2 NW arrays. Up to a 1.5

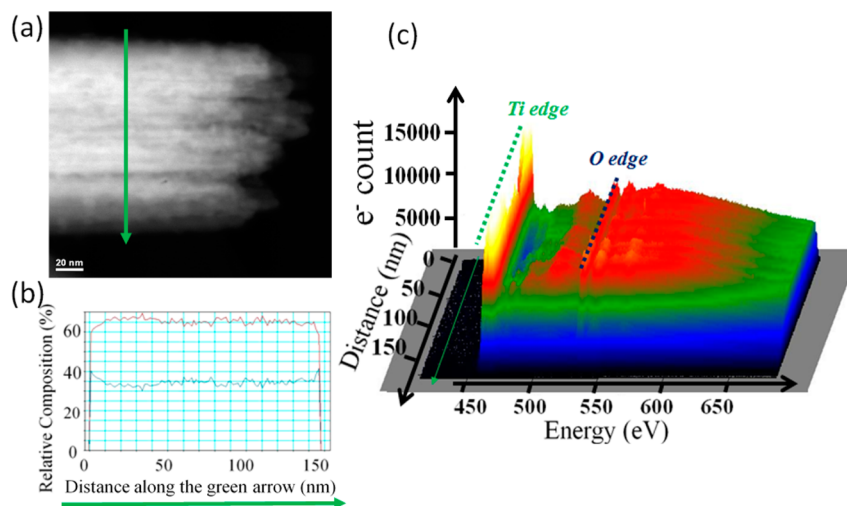**Figure 4.** EELS analysis of a TiO_2@TiO core−shell NW: (a) HAADF-STEM image; (b) EELS relative composition profile; (c) EELS spectrum profiles along the green arrow.
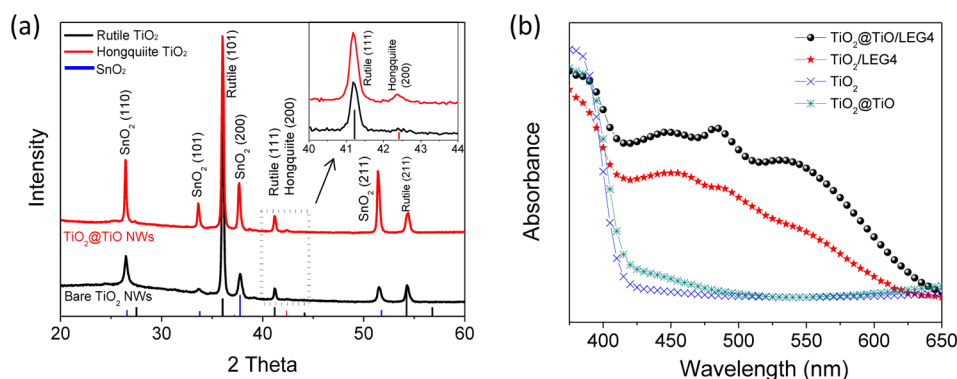

Figure 5. (a) XRD patterns of bare rutile TiO_2 NWs and TiO_2@TiO core−shell NWs. The inset shows the enlargement of XRD patterns in the range 40−44°. (b) UV−vis spectra of bare and dye-loaded TiO_2 and TiO_2@TiO NWs.

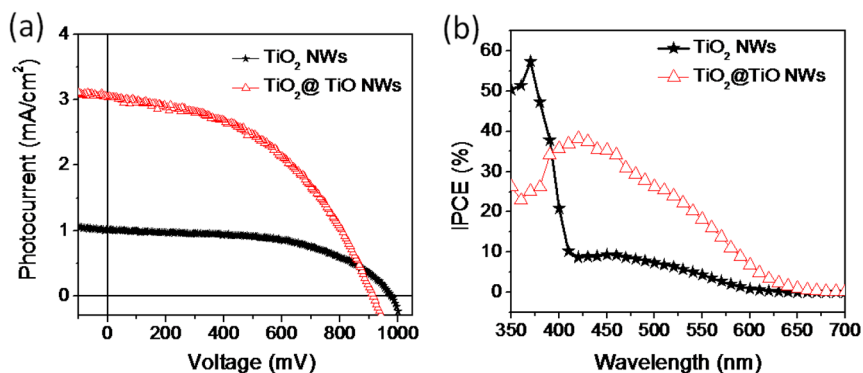**Figure 6.** (a) J−V characteristic and (b) spectra of IPCE under AM 1.5G illumination of DSCs using rutile TiO_2 NWs and TiO_2@TiO core−shell NWs.

Table 1. Photovoltaic Parameters of DSCs Based on 3-μm-Long TiO_2 NWs and TiO_2@TiO Core−Shell NWs

	light intensity (W/m^2)	V_{oc} (mV)	J_{sc} (mA/cm^2)	FF (%)	PCE (%)
TiO_2 NWs	1000	975	1.01	54.1	0.53
TiO_2@TiO NWs	1000	915	3.04	46.7	1.30

absorbance increase was obtained with the presence of the TiO shell. We associated this absorbance increase with the higher

surface roughness introduced by the TiO shell, which provided larger surface areas for dye loading and thus allowed increases in the dye concentration.

The amount of adsorbed dye is the main limitation in NW-based DSCs. Note that the relative density of the 3-μm-long and 150-nm-thick TiO_2 NW arrays used in the present study was around 0.01%, which contrasts with values close to 50% in nanoparticle-based mesoporous films. TiO_2 NW arrays had surface areas 15-fold larger than the flat substrate where they were grown. This value is more than 1 order of magnitude

lower than the surface areas of nanoparticle-based films commonly used for DSCs. Such lower surface areas translated into highly reduced dye concentrations and, therefore, photocurrents. This is the main limitation behind the relatively low overall efficiencies measured from TiO_2 NW-based DSCs compared with those measured from nanoparticle-based TiO_2 DSCs. Higher efficiencies require the use of longer NWs or hierarchical nanostructures.

Still, while a 1.5 increase of the NW array absorbance was measured with the presence of the TiO shell, a 3-fold increase in J_{sc} was obtained from the DSCs. Aside from the increased roughness and thus surface area for dye loading, we believe the TiO shell to play an active electronic role in the DSC performance enhancement. TiO is an n-type semiconductor with a slightly lower band gap than TiO_2, between 2.9 and 3.5 eV (Figure 5b).[32−34] While not too much information regarding the relative positions of the valence and conduction band edges is found in the literature, our results are consistent with a type II band alignment between rutile TiO_2 and hongquiite TiO. This band alignment would favor the injection of electrons from the dye to the NW conduction band, thus leading to increased photocurrents.

CONCLUSIONS

In summary, vertically aligned coaxial rutile−hongquiite TiO_2@TiO core−shell NWs were produced by a two-step hydrothermal−electrochemical deposition process. The coaxial core−shell NWs were used to fabricate DSC devices with cobalt(II/III) redox complexes. Outstanding V_{oc} values above 975 mV were obtained by using the $[Co(bpy)_3]^{2+/3+}$ redox couple as the electrolyte. Meanwhile, the overall energy conversion efficiency increased by a factor 2.5 with the presence of the hongquiite TiO shell. The higher surface area introduced by the rougher TiO shell compared with the smooth TiO_2 surface accounts for part of the photocurrent enhancement. We believe the TiO shell to further improve electron injection from the dye to the TiO_2 NWs.

AUTHOR INFORMATION

Corresponding Authors
*E-mail: cfabrega@irec.cat.
*E-mail: acabot@irec.cat.

Notes
The authors declare no competing financial interest.

ACKNOWLEDGMENTS

REFERENCES

(1) Wang, H.; Bai, Y.; Zhang, H.; Zhang, Z.; Li, J.; Guo, L. *J. Phys. Chem. C* **2010**, *114*, 16451−16455.
(2) Fan, J. D.; Shavel, A.; Zamani, R.; Fábrega, C.; Rousset, J.; Haller, S.; Güell, F.; Carrete, A.; Andreu, T.; Arbiol, J.; Morante, J. R.; Cabot, A. *Acta Mater.* **2011**, *59*, 6790−6800.
(3) Wei, Q.; Hirota, K.; Tajim, K.; Hashimoto, K. *Chem. Mater.* **2006**, *18*, 5080−5087.
(4) Fan, J. D.; Guell, F.; Fabrega, C.; Shavel, A.; Carrete, A.; Andreu, T.; Morante, J. R.; Cabot, A. *Appl. Phys. Lett.* **2011**, *99*, 262102.
(5) Fan, J. D.; Fábrega, C.; Zamani, R.; Shavel, A.; Güell, F.; Carrete, A.; Andreu, T.; López, A. M.; Morante, J. R.; Arbiol, J.; Cabot, A. *J. Alloys Compd.* **2013**, *555*, 213−218.
(6) Fan, J. D.; Zamani, R.; Fábrega, C.; Shavel, A.; Flox, C.; Ibáñez, M.; Andreu, T.; López, A. M.; Arbiol, J.; Morante, J. R.; Cabot, A. *J. Phys. D: Appl. Phys.* **2012**, *45*, 415301.
(7) Ibáñez, M.; Zamani, R.; Gorsse, S.; Fan, J. D.; Ortega, S.; Cadavid, D.; Morante, J. R.; Arbiol, J.; Cabot, A. *ACS Nano* **2013**, *7*, 2573−2586.
(8) Francioso, L.; Taurino, A. M.; Forleo, A.; Siciliano, P. *Sens. Actuators B* **2008**, *130*, 70−76.
(9) Tian, W.-C.; Ho, Y.-H.; Chen, C.-H.; Kuo, C.-Y. *Sensors* **2013**, *13*, 865−874.
(10) Liu, B.; Aydil, E. S. *J. Am. Chem. Soc.* **2009**, *131*, 3985−3990.
(11) Kuang, D. B.; Brillet, J.; Chen, P.; Takata, M.; Uchida, S.; Miura, H.; Sumioka, K.; Zakeeruddin, S. M.; Grätzel, M. *ACS Nano* **2008**, *2*, 1113−1116.
(12) Zou, J. P.; Zhang, Q.; Huang, K.; Marzari, N. *J. Phys. Chem. C* **2010**, *114*, 10725−10729.
(13) Jitputti, J.; Suzuki, Y.; Yoshikawa, S. *Catal. Commun.* **2008**, *9*, 1265−1271.
(14) Wu, H. B.; Hng, H. H.; Lou, X. W. *Adv. Mater.* **2012**, *24*, 2567−2571.
(15) Hwang, Y. J.; Hahn, C.; Liu, B.; Yang, P. D. *ACS Nano* **2012**, *6*, 5060−5069.
(16) Liu, C.; Tang, J. Y.; Chen, H. M.; Liu, B.; Yang, P. D. *Nano Lett.* **2013**, *13*, 2989−2992.
(17) Schrier, J.; Demchenko, D. O.; Wang, L.-W.; Alivisatos, A. P. *Nano Lett.* **2007**, *7*, 2377−2382.
(18) Law, M.; Greene, L. E.; Radenovic, A.; Kuykendall, T.; Liphardt, J.; Yang, P. D. *J. Phys. Chem. B* **2006**, *110*, 22652−22663.
(19) Ibáñez, M.; Zamani, R.; Li, W. H.; Cadavid, D.; Gorsse, S.; Katcho, N. A.; Shavel, A.; López, A. M.; Morante, J. R.; Arbiol, J.; Cabot, A. *Chem. Mater.* **2012**, *24*, 4615−4622.
(20) Li, J. T.; Hoffmann, M.; Shen, H.; Fábrega, C.; Prades, J. D.; Andreu, T.; Hernandez-Ramirez, F.; Mathur, S. *J. Mater. Chem.* **2012**, *22*, 20472−20476.
(21) Chen, H. M.; Chen, C. K.; Chang, Y. C.; Tsai, C. W.; Liu, R. S.; Hu, S. F.; Chang, W. S.; Chen, K. H. *Angew. Chem., Int. Ed.* **2010**, *49*, 5966−5969.
(22) Li, H. X.; Cheng, C. W.; Li, X. L.; Liu, J. P.; Guan, C.; Tay, Y. Y.; Fan, H. J. *J. Phys. Chem. C* **2012**, *116*, 3802−3807.
(23) Zamani, R.; Fiz, R.; Pan, J.; Fischer, T.; Mathur, S.; Morante, J. R.; Arbiol, J. *CrystEngComm* **2013**, *15*, 4532−4539.
(24) Wu, J. M.; Zhang, T. W.; Zeng, Y. W.; Hayakawa, S.; Tsuru, K.; Osaka, A. *Langmuir* **2005**, *21*, 6995−7002.
(25) Fábrega, C.; Andreu, T.; Tarancón, A.; Flox, C.; Morata, A.; Calvo-Barrio, L.; Morante, J. R. *Int. J. Hydrogen Energy* **2013**, *38*, 2979−2985.
(26) Fan, J. D.; Hao, Y.; Cabot, A.; Johansson, E. M. J.; Boschloo, G.; Hagfeldt, A. *ACS Appl. Mater. Interfaces* **2013**, *5*, 1902−1906.
(27) Fan, J. D.; Hao, Y.; Munuera, C.; Garcia-Hernandez, M.; Güell, F.; Johansson, E. M. J.; Boschloo, G.; Hagfeldt, A.; Cabot, A. *J. Phys. Chem. C* **2013**, *117*, 16349−16356.
(28) Straumanis, M. E. *J. Appl. Phys.* **1959**, *30*, 1965−1969.
(29) Yella, A.; Lee, H. W.; Tsao, H. N.; Yi, C. Y.; Chandiran, A. K.; Nazeeruddin, Md. K.; Diau, E. W. G.; Yeh, C. Y.; Zakeeruddin, S. M.; Grätzel, M. *Science* **2011**, *334*, 629−634.
(30) Feldt, S. M.; Gibson, E. A.; Gabrielsson, E.; Sun, L. C.; Boschloo, G.; Hagfeldt, A. *J. Am. Chem. Soc.* **2010**, *132*, 16714−16724.
(31) Huang, Q. L.; Zhou, G.; Fang, L.; Hua, L. P.; Wang, Z.-S. *Energy Environ. Sci.* **2011**, *4*, 2145−2151.
(32) Assim, E. M. *J. Alloys Compd.* **2008**, *465*, 1−7.
(33) Simon, P.; Pignon, B.; Miao, B.; Coste-Leconte, S.; Leconte, Y.; Marguet, S.; Jegou, P.; Bouchet-Fabre, B.; Reynaud, C.; Boime, N. H. *Chem. Mater.* **2010**, *22*, 3704−3711.
(34) Bartkowski, S.; Neumann, M.; Winiarski, A.; Rubie, D. C. *Phys. Rev. B* **1997**, *56*, 10656−10667.

■ NOTE ADDED AFTER ASAP PUBLICATION

This paper was published on the Web on September 11, 2013, with errors in two author names. The corrected version was reposted on September 17, 2013.

9877

dx.doi.org/10.1021/am402344d | *ACS Appl. Mater. Interfaces* 2013, 5, 9872−9877